



Closing the loop between microstructure and charge transport in conjugated polymers by combining microscopy and simulation

Luke Balhorn^a, Quinn MacPherson^b, Karen C. Bustillo^c, Christopher J. Takacs^{d,1}, Andrew J. Spakowitz^{e,f,g,1}, and Alberto Salleo^{a,1}

Edited by Stephen Forrest, University of Michigan-Ann Arbor, Ann Arbor, MI; received March 11, 2022; accepted August 8, 2022

A grand challenge in materials science is to identify the impact of molecular composition and structure across a range of length scales on macroscopic properties. We demonstrate a unified experimental-theoretical framework that coordinates experimental measurements of mesoscale structure with molecular-level physical modeling to bridge multiple scales of physical behavior. Here we apply this framework to understand charge transport in a semiconducting polymer. Spatially-resolved nanodiffraction in a transmission electron microscope is combined with a self-consistent framework of the polymer chain statistics to yield a detailed picture of the polymer microstructure ranging from the molecular to device relevant scale. Using these data as inputs for charge transport calculations, the combined multiscale approach highlights the underrepresented role of defects in existing transport models. Short-range transport is shown to be more chaotic than is often pictured, with the drift velocity accounting for a small portion of overall charge motion. Local transport is sensitive to the alignment and geometry of polymer chains. At longer length scales, large domains and gradual grain boundaries funnel charges preferentially to certain regions, creating inhomogeneous charge distributions. While alignment generally improves mobility, these funneling effects negatively impact mobility. The microstructure is modified in silico to explore possible design rules, showing chain stiffness and alignment to be beneficial while local homogeneity has no positive effect. This combined approach creates a flexible and extensible pipeline for analyzing multiscale functional properties and a general strategy for extending the accesible length scales of experimental and theoretical probes by harnessing their combined strengths.

organic electronics | charge mobility | computational model | electron microscopy

Semiconducting polymers show promise for flexible and printable electronics, displays, and sensors (1). Success in these applications requires an improved understanding of structure-function relationships to create better materials, especially ones with high charge mobility. It is often understood that more-ordered materials yield higher mobility. However, the term "order" is ambiguous and presents itself differently in different high-mobility systems. While some show paracrystalline domains spanning hundreds of nanometers (2), others exhibit order only at short length scales (~10 nm) and yet have high mobility and low disorder (3, 4). Further variables emerge when considering grain boundary structure, molecular conformations, and interchain coupling within the unit cell. Determining the most-important functional elements of order, including their critical length scales for transport and the tradeoffs between them, is essential for designing new materials and improving existing ones. This process requires understanding the systems as a whole, as well as decoupling individual features to learn their importance. Extending our knowledge of hierarchical systems in this way to include mesoscale emergent properties has been identified as a grand challenge in nextgeneration energy materials.

Macroscopic transport is the result of processes occurring over a range of length scales that are coupled to one another. For instance, defects within individual unit cells affect interchain coupling, charge delocalization, and energetic disorder (5). At the mesoscale, transport is sensitive to the geometry of individual chains (6-8), partially due to intergranular transport processes (9). Time-dependent mobility also emerges, with larger structures affecting transport at larger length scales (10). At device scale, long-range alignment leads to anisotropy and associated mobility gains (11, 12). As a result, to be thoroughly understood, transport must be studied across a span of several length scales and time scales, in a manner that bridges and connects phenomena across those regimes.

Several tools exist to probe these length scales individually. Grazing-incidence wide-angle X-ray scattering (GIWAXs) is a staple for bulk-averaged data of molecular order. Polarized

Significance

Semiconducting polymers show promise for flexible and printable electronics, displays, and sensors. We use an experimental map of polymer microstructure to constrain a simulation of polymer chains, creating a model structure that is more detailed across multiple length scales than either method individually. We then simulate charge transport across this structure to study the effects of real-world defects on transport. At short time scales, this model highlights the importance of chain extension and the randomness of charge motion under devicerelevant conditions. At longer time scales, it shows that gradual grain boundaries lead to charge funneling and inhomogeneous charge density. The work also modifies the structure mathematically to explore the importance of chain alignment and geometry and investigate design rules for future materials.

Author contributions: L.B., C.J.T., and A.J.S. designed research; L.B., Q.M., K.C.B., C.J.T., and A.J.S. performed research; L.B., Q.M., C.J.T., and A.S. analyzed data; L.B. wrote the paper; Q.M., K.C.B., C.J.T., A.J.S., and A.S. edited the paper; and A.S. supervised and coordinated

The authors declare no competing interest.

This article is a PNAS Direct Submission.

Copyright © 2022 the Author(s). Published by PNAS. This article is distributed under Creative Commons Attribution-NonCommercial-NoDerivatives License 4.0 (CC BY-NC-ND).

See online for related content such as Commentaries.

¹To whom correspondence may be addressed. Email: ctakacs@slac.stanford.edu, ajspakow@stanford.edu, or asalleo@stanford.edu.

This article contains supporting information online at http://www.pnas.org/lookup/suppl/doi:10.1073/pnas. 2204346119/-/DCSupplemental.

Published November 7, 2022.

X-ray scattering probes longer-range order and has shown that molecular orientational correlation lengths on the order of a few hundred nanometers are correlated with high mobility (13). On the theory side, models have elucidated the effects of energetic disorder (14), molecular conformations (6, 8), and grain boundary structure (7). However, there are still two important gaps to fill. First, the length scale at tens of nanometers, influenced by both grain boundaries and molecular conformations, is difficult to probe with existing techniques. Many models ignore microstructure or treat it phenomenologically. Second, it is currently difficult to apply models to experimental microstructures and learn their importance. There is a need for a closed-loop interpretation that evaluates experimentally determined morphologies using a theoretical approach, disentangling the intrinsic properties of the single molecule and the contributions of mesoscale organization.

A prime candidate for probing microstructure is transmission electron microscopy (TEM). In recent years, much progress has been made in studying conjugated polymers via low-dose TEM to sidestep the effects of beam damage (15, 16). Techniques of high-resolution TEM (HR-TEM) and spatially resolved electron nanodiffraction (4D-STEM) (17) have been used to map the orientation of polymer crystallites and their connections to one another (18). The strength of these techniques in soft materials science is to connect multiple length scales: local order, mesostructure, and device-level microstructure.

To apply a charge transport model to observed microstructures, an additional length scale must be added: that of molecular geometry, which plays an important role in charge transport. TEM cannot generally discern the structure of individual chains due to dose limitations for soft materials. We bridge this gap by using the experimental data to constrain the configurations of the polymers at the molecular scale. We assume that the polymer behaves locally as a liquid crystal, so molecules are energetically rewarded for aligning with their neighbors. The average direction of these neighbors at each location is known from TEM. Thus, we use TEM to estimate the strength and direction of the aligning energy field at each point and simulate chain geometries within that energy landscape. The chains generated in this manner are consistent both with the diffraction data and with the molecular thermodynamic behavior of polymer chains. The new structure can now support a theoretical probe that spans length scales from single chains to mesoscale and treats mesoscale structures and defects in more detail than our past structural models (7, 9, 19). By using theory to calculate molecular conformations, our method goes beyond morphology-directed coarse-graining methods in making general and far-reaching predictions (20).

Charges are simulated moving across the generated structures using a biased random walk that favors on-chain hopping. Transport simulations span multiple length scales—from individual chains to hundreds of nanometers—to show effects of both molecular geometry and microstructure. The structure is studied as is to see the effect of real defects and is also modified in silico to explore improvements for future materials. The concurrent ability to use real microstructures but also to modify them in silico brings insights into design rules for charge transport. In short, this work unites physical understanding with experimental constraints, increasing structural knowledge across multiple length scales and yielding a powerful tool for exploring structure-function relationships in charge transport.

Results

The alignment strength and direction for a film of poly[2,5bis(3-tetradecylthiophen-2-yl)thieno[3,2-b]thiophene] (PBTTT)

are estimated at each point using electron nanodiffraction patterns gathered via 4D-STEM (16, 17, 21). The process of combining diffraction patterns into an interpolated map of chain direction is shown in Fig. 1. Lines are drawn perpendicular to the pi-stacking direction, so they represent the direction of polymer chains in each region.

Fig. 2 compares the director field computed from electron diffraction to the structure of simulated chains. In Fig. 2A, line direction shows the average direction of polymer chains as inferred from electron diffraction, and line intensity represents the strength of diffraction signal. The resulting structural map shows large grains, gradual grain boundaries, and disclinations resulting from annealing the film in a liquid crystalline phase. In Fig. 2B, black lines show a sample of polymer chains in each region. In Fig. 2 A and B, the color shows the average alignment direction in each region. The common color pattern helps to compare the original and final alignment maps. For example, both have a purple "U" shape near the top and a blue region in the lower left. The individual black lines in Fig. 2B show that, while polymers tend to extend in the alignment direction, they are far from straight due to entropic effects. Both frames also show anisotropy: more horizontal domains are present than vertical domains. This is due to sampling variation, since domains are large relative to the field of view. Fig. 2C shows a schematic of a single chain and also defines some rates for the charge transport model.

Fig. 3A shows a top-down projection of a single polymer chain. Under the influence of an applied field, charges tend to move to the right side of the chain, seeking beads with the lowest potential. Since on-chain moves occur about 1,000× more often than interchain moves, occupancy probabilities tend to approach the long-time limit before an interchain hop occurs. Due to entropy, even the higher-energy sites have a significant chance of being occupied. Consider a field strength of 1 V/µm, which is a high but reasonable lateral field strength in many organic field-effect transistors (OFETs). The maximum potential difference for the chain shown is just 13 mV, compared with an average thermal energy of 25 meV, meaning that charges are just twice as likely to be found on the right edge as the left edge. This ratio increases as chains span more distance in the field direction: the most-extended chains have a potential difference of 45 mV and an occupancy ratio of 6:1, increasing the tendency of charges toward forward motion. Thus, while a majority of charges occupy the low-energy end of the chain, a significant portion occupy the high-energy end, even at long time and relatively high field.

Observing the magnitude of these drift-diffusion interactions under device-relevant conditions helps to form a better mental model of charge transport. We define a distance d as the distance a charge moves along a chain between two interchain-hopping events, in the direction of the electric field. A histogram of these distances is shown in Fig. 3B for simulations at different field strengths. The chosen field strengths represent "moderate", "high", and "extreme" field strengths for OFETs; for example, it is not uncommon to impose a source-drain voltage of 5 V over a 10-µm channel. At field strengths of 0.1 and 1 V/µm, charges are nearly as likely to move backward as forward and the mode of the distribution is near 0 nm. The potential difference along the chain creates a slight shift in the distribution, and this shift accounts for all net forward motion. The distribution of moves becomes more asymmetric at 10 V/µm as large backward moves become less common, but the mode remains near 0 nm. The expected values for forward motion are shown in Fig. 3C. For all three cases, the net forward motion per chain is a few nanometers or less.

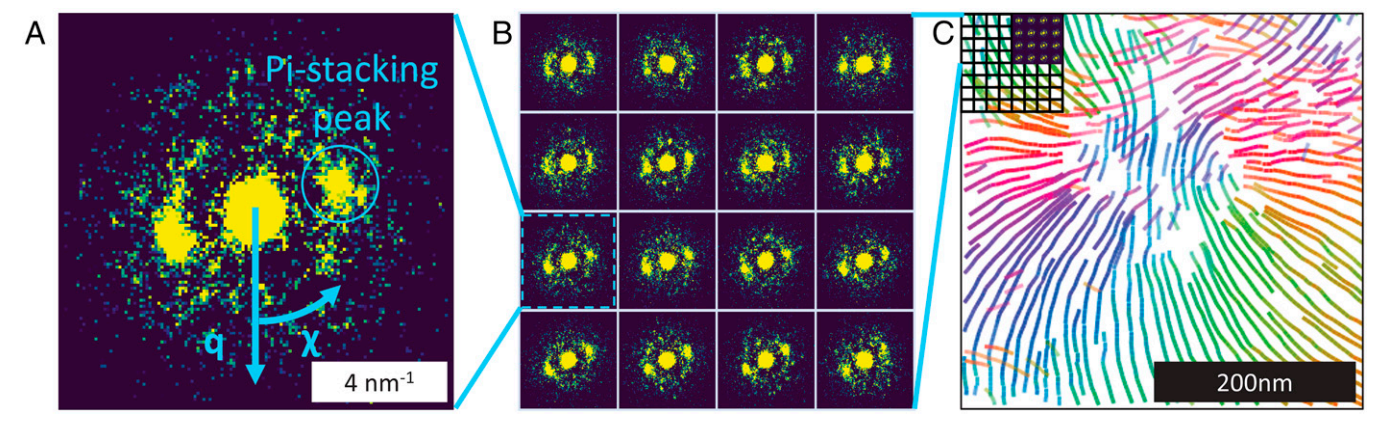


Fig. 1. Building an alignment map. A shows the electron diffraction pattern at a single location. The 010 diffraction peak at 2.8 nm⁻¹ lies parallel to the substrate and perpendicular to the chain direction, yielding chain orientations. B shows an array of these patterns, collected 10 nm apart and showing local fluctuations in the crystal alignment. C shows how these patterns are interpolated into a flow plot, where line direction and color indicate chain direction and line intensity represents diffraction intensity.

Interchain hopping limits forward progress and produces two time regimes of charge transport, both affected by local microstructure. Fig. 4A shows charge mobility as a function of time at 1 V/µm applied field. Starting positions for charges covered a 400 × 800 nm area to sample a wide range of structures. The vertical line shows the interchain hopping time, defined as 1/k_{hop}. Below the interchain hopping time, on-chain hopping dominates. In agreement with past work, the highest mobility values occur in the first nanosecond, when charges can move along chains unobstructed (10, 19). After this time, chain ends prevent more forward progress, leading to a drop in mobility. Charges cannot continue forward until an interchain hop occurs. Above the interchain hopping time, the mobility reaches a plateau. Since interchain hopping in our model is geometry independent, all forward progress still occurs due to on-chain hopping, with interchain hopping allowing charges to bypass chain ends. The roll off at the end of this plateau occurs when about 80% of test charges have fully crossed the region of interest, so only slower charges remain and contribute to the mobility.

In both time regimes, chain alignment impacts forward progress. In Fig. 4 B and C, charge mobility in each region is averaged over the first nanosecond of transport, where most charges move short distances along single chains. For each applied field angle, the regions with the highest mobility are those with chains that are parallel to the applied field, while the regions with the lowest mobility have chains perpendicular to the applied field. Thus, regions that have a high mobility for one direction tend to have a lower mobility for the other. The 0° case has a higher density of high-mobility regions, leading to a larger mobility overall. Quantitatively, 59% of chains have more horizontal than vertical character, leading to an anisotropy ratio for the entire region of 1.2 for short times and 1.3 for long times. For comparison, macroscopically aligned edge-on PBTTT has shown an anisotropy ratio of up to 10 (12).

In light of the single-chain analysis in Fig. 3, why should chain alignment in the field direction increase charge mobility? First, as the chain becomes more parallel to the electric field, the potential difference between the two chain ends increases, leading to a larger probability of a charge occupying the forward side of the chain when an interchain hop occurs. Second, chains that are more parallel to the field have a larger component of their charge motion in the field direction. The first effect is exponential with chain extension, making it the more significant of the two, while the second effect is proportional to chain extension.

Long-time transport simulations highlight repeatable microstructural heterogeneity at device-relevant length scales. Fig. 5 shows a simulation in which test charges are placed on one side of the region of interest, then move toward the other side under an applied electric field, reminiscent of time-of-flight measurements. Snapshots in Fig. 5 A-F help to illustrate charge motion, while Fig. 5G shows average charge density over all time. As charges are pushed across the region by the electric field, they are influenced by the orientations of polymer chains in each region. Microstructural features funnel charges into some regions and away from others. In some cases, they are guided to regions where chains are mostly perpendicular to the electric field, even if a different route would have fewer obstacles overall.

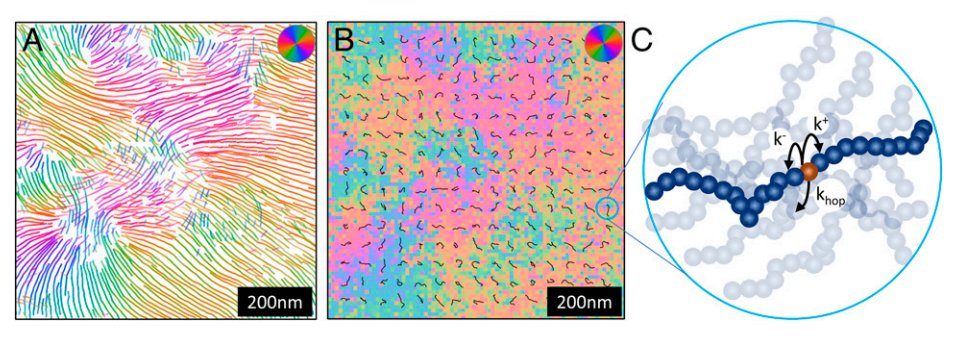


Fig. 2. Generating chains. A shows the crystal alignment of the sample interpolated from electron diffraction data. Color and line direction show the direction of polymer chains, and line intensity represents the intensity of diffraction. B shows simulated chains based on the chain directions and intensities from A. C shows a schematic of one simulated chain, highlighting the discretization of the chain into beads and the mechanisms included in our transport model.

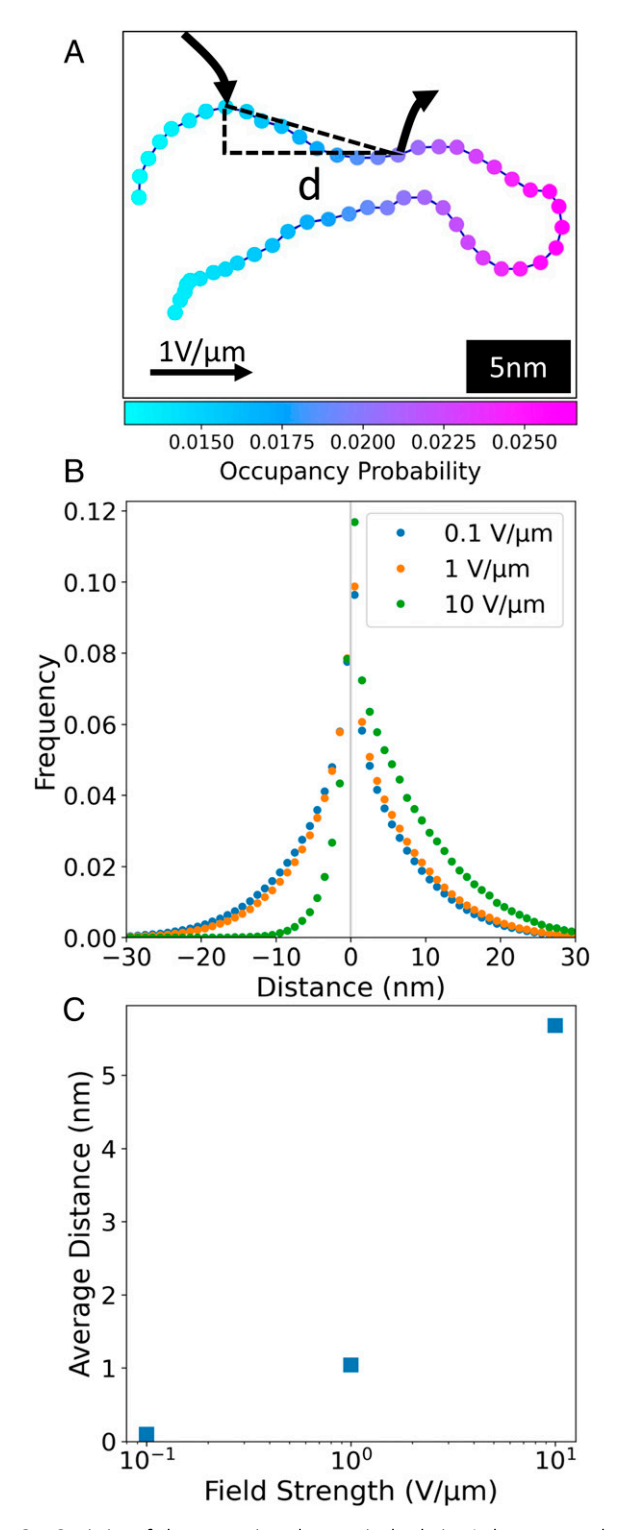


Fig. 3. Statistics of charge motion along a single chain. A shows a top-down view of a polymer chain, color coded by computed occupancy probability in the limit of long time (about 100 ns) for a field strength of 1 $V/\mu m$. The field creates a potential difference of 13 mV between the left and right sides of the polymer, so that charges are twice as likely to occupy beads on the right side of the chain as the left side. A distance d is defined, which is the distance a charge travels between entering and leaving the chain, relative to the field direction. B shows distributions in d for simulations using all chains and three different field strengths (n = 8,000 charges). d can be positive or negative and has a mode near zero for all distributions. C shows the expected value of forward progress for each of these distributions (n = 8,000 charges).

Fig. 5H shows the time for charges to fully cross the region of interest at various applied field strengths. Within each experiment, the finishing times of individual charges vary widely, following a lognormal distribution. Both the mean and spread of finishing time increase as electric field decreases. At 0.1 V/ μm, a device-relevant field strength, charges move only twice as fast as they do for pure diffusion.

Funneling effects created by the microstructure are especially clear in video form and are explored for multiple field directions in Videos S1-S5. Charges are guided along different pathways, depending on the applied field angle, leading to different regions having the highest integrated charge

Charges spend much more time in some regions than others due to funneling effects of the microstructure. This effect is further quantified in Fig. 6 by integrating carrier density over all time in each 10×10 nm spatial bin. For the $10 \text{ V/}\mu\text{m}$ case, for example, the 10% most-visited bins have 31% of the charge density, meaning they are visited three times more than the average bin (see the dotted blue lines). Similarly, the 37% leastvisited bins have just 10% of the carrier density (these carrier densities are integrated over long times, so they do not indicate a highly inhomogeneous charge density, which would lead to strong internal fields). Fig. 6 B-D show maps of integrated carrier density at 0.1, 1.0, and 10 V/μm, respectively. Inhomogeneity in carrier paths generally increases with increasing field strength, since the driving force to follow chains becomes stronger and charges have less time to diffuse. Comparing with Figs. 3 and 4, the most-visited regions are often regions with lowerthan-average alignment in the field direction, leading to a reduction in average forward progress and therefore a reduction in charge mobility. The curves created by disclinations produce both a funnel and a blockage when charges approach from the concave direction.

Simulated chains are now modified in silico in ways that are difficult to achieve experimentally, in order to explore the effect of different strategies for improving a system. Three different types of modifications are explored in Fig. 7. First, chains can be made rigid, keeping their orientations constant while replacing their shapes with rigid rods. Chains can also be aligned, keeping their shapes constant while changing their orientations to match the angle of the electric field. Finally, chains can be shuffled, keeping their shapes and orientations constant while swapping their positions with one another. Shuffling chains keeps the average alignment of the entire region constant while destroying mesoscale structures and defects. Each of these modifications can either be applied to all chains or a fraction of chains. The effects of these changes on charge mobility and distance traveled per chain are shown in Fig. 7E.

Aligning chains and making them rigid both increase charge mobility. These modifications have two effects: they increase the potential difference between the two ends of the chain and they increase the maximum distance a charge can travel before an interchain hop occurs, the first effect being the more significant of the two. Applying these effects to a fraction of chains has a benefit proportional to the fraction of chains affected. Interestingly, aligning chains perfectly with the field while maintaining their conformation has a relatively modest effect on mobility for this system (factor of 1.6). Stretching the chains, irrespective of their orientation in the field direction, has a much-larger effect (factor of 3.1). More surprisingly, shuffling chains does not decrease mobility but rather slightly improves it.

Discussion

Mesoscale structure is shown to have several consequences for charge transport in this material, which are consequences of the

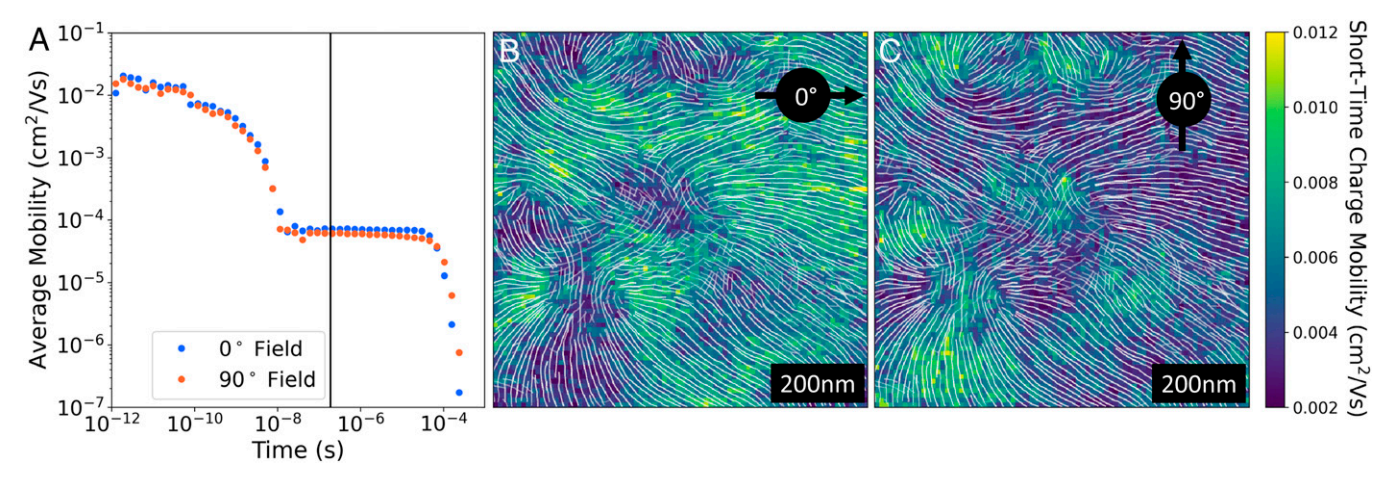


Fig. 4. Short-time transport. A shows time-dependent charge mobility at 1 $V/\mu m$ for two directions of applied field (n = 800,000 charges). The vertical line shows the average interchain hopping time. B and C show the spatially resolved hole mobility of the region of interest, computed over the first nanosecond of transport. White lines are overlaid on these images to show chain direction in each region.

chains and smaller regions that combine to create mesoscale structure. Local anisotropy influences lateral motion of charges, funneling them toward some regions of the film and away from others. The way charges interact with microstructural features and defects is dependent on both the angle and the polarity of the applied field, making it difficult to represent the film as a simple network of transistors. Charge pathways also change as field strength increases, increasing the inhomogeneity in transport participation.

A particularly important observation is that the large domains and gradual boundaries and disclinations of this material's mesostructure may create morphologies detrimental to transport. Charges are often funneled to regions with chains oriented perpendicular to the field, particularly at high field strengths. These

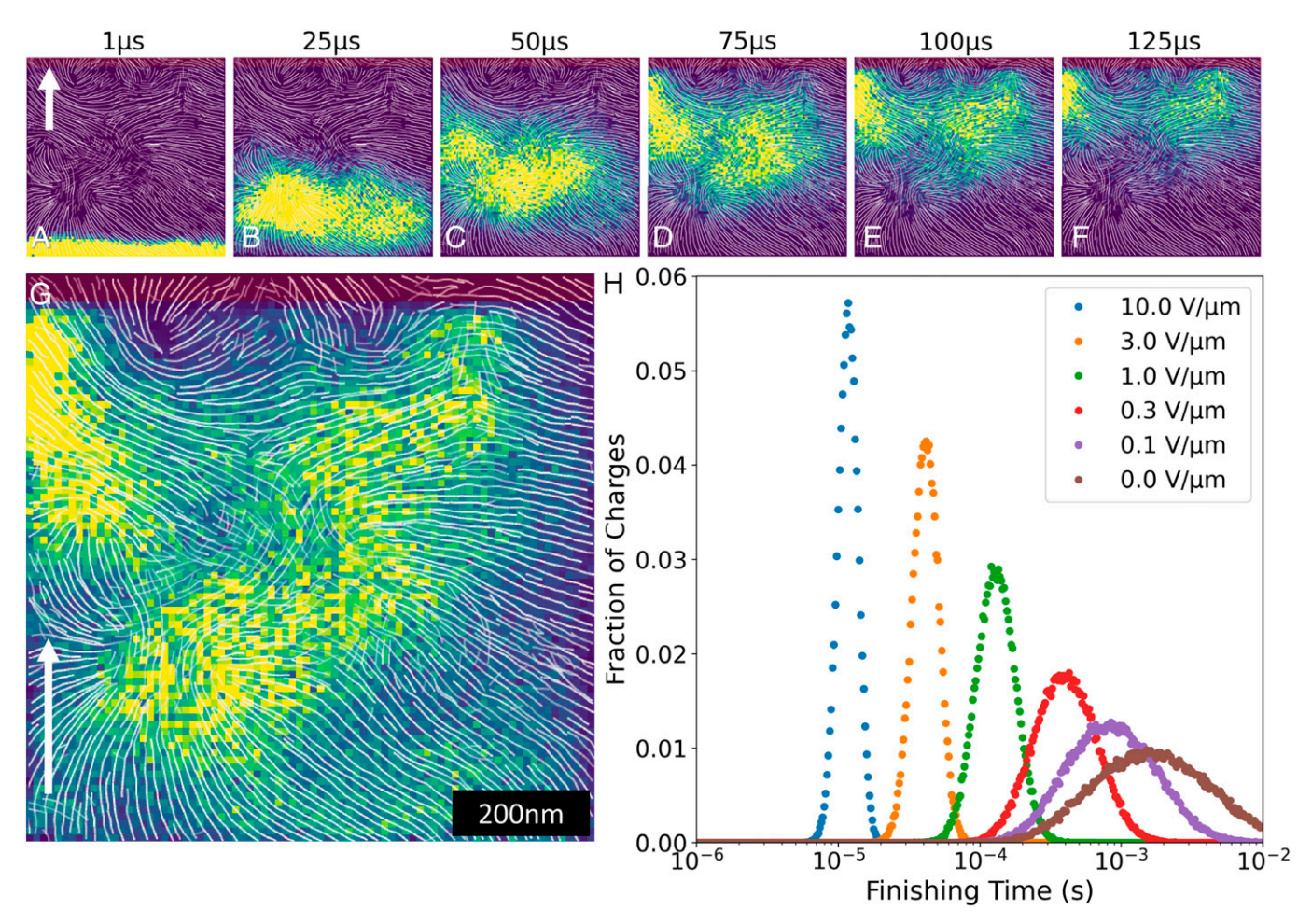


Fig. 5. Simulated charge trajectories. A-F show snapshots of the charge density across the film at various times. Charges were placed on the lower wall of the region, then a field of 1 V/µm was applied to push charges toward the absorbing upper boundary. Image widths are 800 nm. G shows the average time spent at each location over all time. All charge density maps are overlaid with white lines to show local chain direction and a red field to show the absorbing boundary. H shows distributions of crossing time at various field strengths. n = 80,000 charges for all frames.

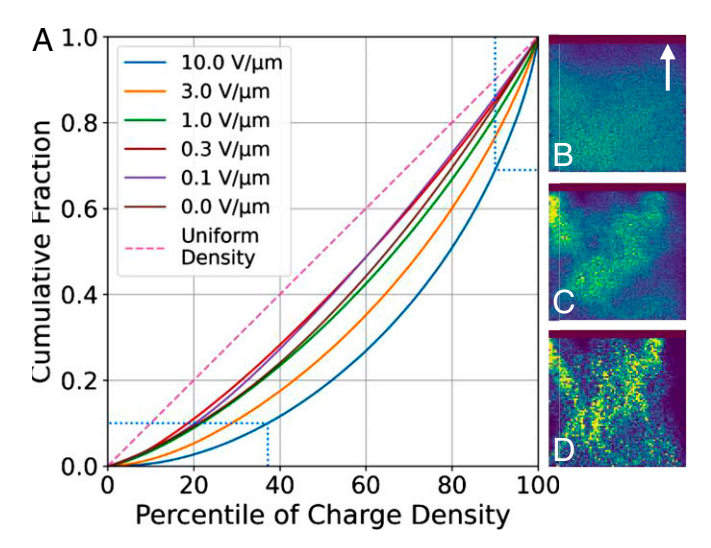


Fig. 6. Heterogeneity in charge density. A shows the cumulative fraction of charge density at various percentiles, where individual units are 10 \times 10 nm bins, for various applied electric fields. A diagonal line represents a completely homogeneous result, and increased curvature represents increased inhomogeneity. The two blue boxes are used in example calculations. $B\!-\!D$ show maps of integrated charge density of simulations at 0.1, 1.0, and 10 $V/\mu m$, respectively. Red overlays show the absorbing boundary. n = 80,000 charges for all frames.

defects reduce the distance traveled per chain and therefore generate a transport penalty that may overwhelm any benefits generated by the gradual nature of the original mesostructure. In contrast, shuffled microstructures lack the large, uniform regions that lead to charge funneling and its detrimental effects.

If large homogenous domains do not improve transport, why is annealing beneficial for charge mobility in PBTTT? When ordered domains form and increase in size, individual chain geometries also change, becoming straighter on average. This creates more forward progress between interchain hops, leading to proportional gains in mobility. The larger domains are not valuable in themselves but are a means to the end of stretching chains. It is also possible that annealing changes intermolecular interactions on length scales under 10 nm, which are not captured by this model. In particular, such changes could change interchain hopping rates or the quantity of energetic traps. This particular property of crystals may be molecule dependent. For instance, in poly(3-(2'-ethyl)hexylthiophene), mobility increases upon crystallization and yet charges are inherently localized on a single chain, suggesting that the beneficial effect of crystallization is purely conformational (22, 23).

Our model suggests improving the drift velocity requires either improving the distance charges move along each chain or the interchain hopping rate. Further, it suggests that the distance moved along a single chain is best improved by stiffening that chain, having an even larger effect than aligning the chains in the field direction. Thus, we propose relatively long and stiff chains with high interchain coupling as a target for synthesizing new materials in this space.

Conclusions

A grand challenge in materials science is to understand the interplay between mesoscale and molecular order on macroscopic functional properties. By self-consistently incorporating experimental and thermodynamic properties, we demonstrate a holistic framework that enables a detailed, multiscale understanding of charge transport properties. These coordinated efforts reveal the impact of spatial heterogeneity on charge migration and offer insight into the rate, efficiency, and anisotropy in charge transport pathways. Additionally, we explore how modulating the degree of order, spatial correlation, and chain alignment affect charge transport.

Furthermore, this work creates a pipeline for studying the impact of structure on charge transport across polymer systems. A wide range of polymers can be imaged using 4D-STEM or related techniques to estimate local molecular orientations and simulate chains. Within the same material, the effects of different microstructures, chain configurations, and defects can be explored, using a synergistic mix of experimental samples and

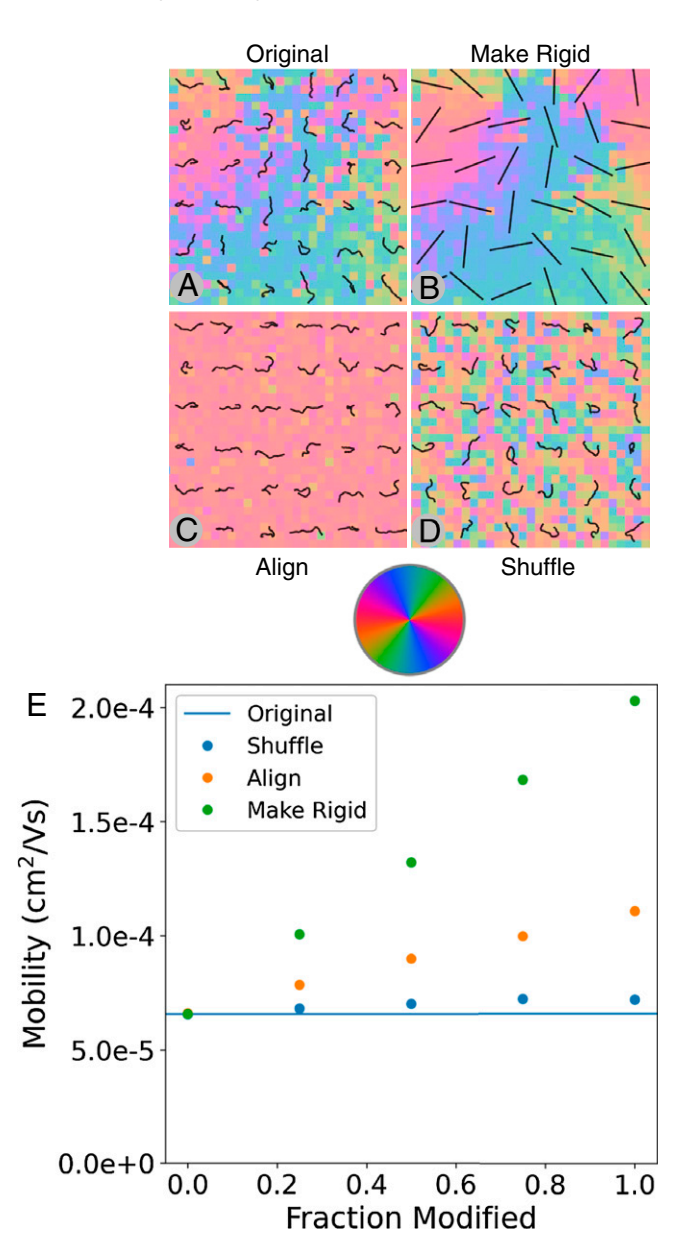


Fig. 7. Impact of structural modifications. A shows the original structure, while B-D show three different types of modifications and their effect on the original chains. Black lines show a sample of individual chains, while the background color shows the average alignment direction in each region. To make chains rigid, the angle of chains is kept constant, but their shape is replaced with rigid rods. To align chains, their shape is kept constant, but their angle is changed to be horizontal. To shuffle chains, their shape and angle are kept constant, but their positions are swapped with one another. Each of these modifications can be applied either to all chains or some fraction of chains. E shows the charge mobility and distance traveled per chain for each modification applied to various fractions of chains (n = 8.000 charges).

in silico variations. When necessary, more complexity can be added to the model to capture materials that do not meet our current assumptions. Other properties that depend on both mesoscale structure and chain geometry, such as physical and thermal properties, can be probed using our structural model as a foundation. These fundamental insights lay a foundation for closing the structure-property loop across multiple length scales, guiding the experimental fabrication of optimal conducting polymer materials and devices.

Materials and Methods

Film Preparation. Solutions of the polymer PBTTT (Mn = 28 kDa, Imperial College) are prepared at 2 mg/mL in chlorobenzene and stirred 24 h at 80 °C. Films are spin cast 800 rpm on silicon nitride TEM windows to produce films 30 nm thick, then annealed in PBTTT's liquid crystalline phase at 180° for 2 h. Both casting and annealing occur in a nitrogen glovebox. This process produces edge-on crystallites with aligned domains of roughly 200 nm and gradual grain boundaries. In this edge-on configuration, the lamellar stacking is parallel to the substrate such that the pi-pi stacking arising from the conjugated parts of the polymer chain is in plane and perpendicular to the electron beam. This combination of material and processing conditions was chosen because it is well studied and displays both high crystallinity (which helps signal to noise) and a high degree of texture (which reduces error from tilted crystallites). Samples were also vapor doped with 2,3,5,6-tetrafluoro-7,7,8,8-tetracyanoquinodimethane postannealing as part of another investigation (see SI Appendix).

TEM. An 80×80 grid of electron diffraction images spaced 10 nm apart covers the region of interest, as shown in Fig. 1 A and B. A convergence angle of 0.48 mrad produced a spot size of 2.5 nm (full width at half-maximum). Average dose was 600 $e^{-}/Å^{2}$, with a dose in the central spot of up to 10,000 $e^{-}/Å^{2}$. From past X-ray diffraction data, an in-plane peak is expected to appear at 2.8 nm^{-1} (q = 1.8 Å^{-1}) in low-dose 4D-STEM, which corresponds to a real space dimension of about 3.5 Å. This is known as the pi-stacking peak and marks a crystallographic direction perpendicular to the chain direction. X-ray diffraction also shows that samples adopt a high degree of crystallographic texture with respect to the substrate (SI Appendix, Fig. S1), allowing electron diffraction to provide a useful estimation of the local orientational order.

Structural Model. Chain geometries are generated using a Monte Carlo simulation, building upon the methods used previously by this group (7-9, 19) while adding capabilities for experimental integration. To define our system, we represent polymer chains as strings of beads. The spacing between beads is 1 nm, which roughly corresponds to the size of one repeat unit. The measured region of the film is $800 \times 800 \times 30$ nm and contains over five million repeat units. For computational viability, 10% were modeled, so that the areal density matches the bottom 3 nm of the film—the portion active in field-effect transistors. Next, we define the total energy function of the polymer system. This energy is composed of three terms: bending energy, chain alignment, and compressibility. First, the bending energy of the system is given by the wormlike chain model, which is commonly expressed as

$$E_b = \frac{1}{2} k_B T I_p \sum_{i=1}^{N_c} \int_0^L \left(\frac{\partial^2 \vec{r}_{i}(s)}{\partial s^2} \right) ds,$$
 [1]

where E_b is the bending energy, k_BT is thermal energy, I_p is the persistence length, i is the chain index, N_c is the No. of chains, L is the contour length, $\vec{r}_i(s)$ is the position vector at distance s along chain i, and s is the distance along the chain. The second derivative term gives the magnitude of curvature at each point along the chain. Applying the wormlike chain model to a discretized chain requires additional care to preserve the ability of chain segments to bend and shear. The corrected bending energy is given by

$$E_{b} = \sum_{i=1}^{N_{c}} \sum_{j=1}^{N} \frac{\varepsilon_{b}}{2\Delta} \left| \vec{u}_{i,j} - \vec{u}_{i,j-1} - \eta \vec{R}_{i,j}^{\perp} \right|^{2} + \frac{\varepsilon_{\parallel}}{2\Delta} \left(\vec{R}_{i,j} \cdot \vec{u}_{i,j-1} - \Delta \gamma \right)^{2} + \frac{\varepsilon_{\perp}}{2\Delta} \left| \vec{R}_{i,j}^{\perp} \right|^{2},$$
[2]

where j is the bead index, N is the No. of beads, $\vec{R}_{i,i}$ is the vector connecting bead j and bead j-1 along chain i, $\vec{u}_{i,j}$ is the orientation of bead j on chain i,

 $ec{R}_{i,i}$ is the component of the interbead vector in the direction of the bead orientation vector, and Δ is the discretized segment length (24). Other constants, including the bending modulus ε_h , stretch modulus ε_{\parallel} , shear modulus ε_{\perp} , bend-shear coupling η_i and fractional ground-state segment length γ_i are derived from wormlike chain theory, so that the only independent parameters needed are the persistence length and the discretization length (25). Persistence length for PBTTT is estimated as 9.0 nm (26).

The second energy term comes from liquid crystal alignment. Polymer molecules tend to align with one another, and this tendency can be expressed as a quadrupole energy field using the equation

$$E_{a} = \sum_{i=1}^{N_{c}} \sum_{j=1}^{N} -A(\vec{r}_{i,j}) \cos^{2}[\theta_{i,j} - \theta(\vec{r}_{i,j})],$$
 [3]

where E_a is the alignment energy, $\vec{r}_{i,j}$ is the position of bead j on chain i, $\theta_{i,j}$ is the angle of that bead, $A(\vec{r}_{i,i})$ is the strength of the aligning field at that bead's position, and $\theta(\vec{r}_{i,i})$ is the angle of the aligning field at that position. Normally, the energy field is recalculated after each step of a simulation using the mean and variance of chain alignment in each region. In this study, however, the final alignment is inferred from TEM data and is used to estimate the self-aligning energy field. The angle of the field at each point is set equal to the angle of polymer chains as inferred from diffraction data, and the strength of the field is set proportional to the local pi-stacking peak intensity.

The third energy term reduces the compressibility of the system so that structural features do not have a disproportionate effect on density. Compressibility is applied by splitting the region into cubic bins with side length of 10 nm and comparing the density of each bin with the density of the entire system. Deviations from the average density receive an energy penalty using the equation

$$E_{C} = \sum_{b=1}^{N_{b}} \kappa \left(\rho_{b} - \overline{\rho} \right)^{2},$$
 [4]

where E_C is compressibility energy, b is the bin index, N_b is the No. of bins, ρ_b is the density of bin b, $\overline{\rho}$ is the average density among all bins, and κ is the inverse of compressibility. For this simulation, the resulting rms density variation is near 25%.

Over the course of the structural simulation, trial moves are proposed that bend, slide, or rotate different portions of a polymer chain. The energy change for each trial move is calculated. Moves with negative energy changes are always accepted, while moves with positive energy changes are sometimes accepted, with probabilities given by the equation

$$P = \begin{cases} 1 & \text{if } \Delta E \le 0\\ \exp\left(-\frac{\Delta E}{k_B I}\right) & \text{if } \Delta E > 0 \end{cases}$$
 [5]

where P is the acceptance probability, ΔE is the change in energy $(\Delta E_A + \Delta E_B + \Delta E_C)$, and $k_B T$ is thermal energy. Accepting some unfavorable moves is necessary to represent entropy in the system. To avoid high-energy local minima, multiple simulations are run in parallel with one parameter modified and structures are periodically swapped between the simulations, in a scheme known as parallel tempering. For this study, the proportionality constant between local diffraction intensity and aligning field is the varied parameter, which conveniently allows us to explore the sensitivity of the results to degree of alignment.

Overall, this structural model self-consistently adds information from an experimental director field to generate chains consistent with that data. Since this method relies on few assumptions, it is applicable to a variety of polymer systems. The key requirements are that the chain orientation is detectable using 4D-STEM or another spatially resolved microscopy technique, that few overlapping grains are present in the out-of-plane direction, and that the self-aligning tendency of the polymer chains can be mathematically expressed.

Charge Transport Model. Each bead from the polymer chains simulated above acts as a discrete location that can be occupied by a charge carrier. Charge carriers in PBTTT are holes, but these results are expected to represent both n-type and p-type polymers. Charges can move to adjacent beads on the same chain or hop between chains (Fig. 2C). Since the on-chain hopping rate is roughly 1,000× higher than the interchain hopping rate, the on-chain hopping is treated in detail while the interchain hopping can be simplified to improve computation. The interchain hopping rate is treated as geometry independent and therefore is the same at all points. The rate of change of occupancy probability on a particular bead I can then be described by the differential equation

$$\frac{dp_i}{dt} = -p_i(k_{hop} + k_i^+ + k_i^-) + p_{i+1}k_{i+1}^- + p_{i-1}k_{i-1}^+,$$
 [6]

where p_i is the probability of bead i being occupied, k_{hop} is the interchain hopping rate, k_i^+ and k_i^- are the rates of forward and backward charge motion starting at bead i, and t is time. Solving this system of differential equations, the probability of each bead being occupied at time t is given by

$$\rho_i(t) = \sum_{j=1}^{N} \left\{ \exp[-(\mathbf{K} + \mathbf{I} k_{hop})t] \right\}_{ij} \rho_j(0),$$
 [7]

where **K** is a matrix of on-chain hopping rates (*SI Appendix*, Eq. **S4**) and $p_j(0)$ is the probability of each site being occupied at t=0. In the common situation where a charge starts at a specific point on a chain, the probability at that point would be 1 and the rest would be 0. Finally, contributions from on-chain and interchain transport are separated, yielding

$$\rho_i(t) = \exp(-k_{hop}t) \sum_{j=1}^{N} \exp(-\mathbf{K}t)_{ij} \ \rho_i(0).$$
 [8]

The exponential decay term describes interchain transport, while the matrix exponential describes on-chain transport.

Now that the problem has been solved symbolically, the inputs k_{hop} and **K** are determined from by Marcus theory (27) using the equation

$$k_{ij} = \frac{2\pi}{\hbar} \frac{J_0^2}{\sqrt{4\pi\lambda_0 k_B T}} \exp\left[-\frac{(\lambda_0 + \Delta G_{ij})^2}{4k_B T \lambda_0}\right],$$
 [9]

where ΔG is the difference in energy of the two sites. For on-chain hopping, ΔG is determined by the charge's location in the electric field. For interchain hopping, we use an aggregate value for ΔG given by

$$\Delta G = Fel_{inter}$$
 [10]

where *F* is the applied field, *e* is elementary charge, and *l*_{inter} is the characteristic spacing for interchain transport. When an interchain hop occurs, all sites that neighbor the charge have an equal probability of receiving it. For the materials parameters in Eqs. **9** and **10**, we use experimentally fit values of another semiconducting polymer, spirobifluorene (19). Due to differences between this polymer and PBTIT, as well as other approximations, this work is not intended to reproduce experimental mobilities of PBTIT. However, the goal is to understand

- W. S. Wong, A. Salleo, Flexible Electronics: Materials and Applications (Springer Science & Business Media. 2009), vol. 11.
- J. Rivnay et al., Structural origin of gap states in semicrystalline polymers and the implications for charge transport. Phys. Rev. B Condens. Matter Mater. Phys. 83, 121306 (2011).
- X. Zhang et al., Molecular origin of high field-effect mobility in an indacenodithiophene-benzothiadiazole copolymer. Nat. Commun., 1–9 (2013).
- D. Venkateshvaran et al., Approaching disorder-free transport in high-mobility conjugated polymers. Nature 515, 384–388 (2014).
- H. Yamagata, F. C. Spano, Interplay between intrachain and interchain interactions in semiconducting polymer assemblies: The HJ-aggregate model. J. Chem. Phys. 136, 184901 (2012)
- D. S. Pearson, P. A. Pincus, G. W. Heffner, S. J. Dahman, Effect of molecular weight and orientation on the conductivity of conjugated polymers. *Macromolecules* 26, 1570–1575 (1993).
- S. A. Mollinger, A. Salleo, A. J. Spakowitz, Anomalous charge transport in conjugated polymers reveals underlying mechanisms of trapping and percolation. ACS Cent. Sci. 2, 910-915 (2016).
- P. E. Rudnicki et al., Impact of liquid-crystalline chain alignment on charge transport in conducting polymers. Macromolecules 52, 8932–8939 (2019).
- S. A. Mollinger, B. A. Krajina, R. Noriega, A. Salleo, A. J. Spakowitz, Percolation, tie-molecules, and the microstructural determinants of charge transport in semicrystalline conjugated polymers. ACS Macro Lett. 4, 708-712 (2015).
- A. Devižis, K. Meerholz, D. Hertel, V. Gulbinas, Hierarchical charge carrier motion in conjugated polymers. Chem. Phys. Lett. 498, 302–306 (2010).
- M. J. Lee et al., Anisotropy of charge transport in a uniaxially aligned and chain-extended, high-mobility, conjugated polymer semiconductor. Adv. Funct. Mater. 21, 932–940 (2011).

what aspects of the structure are most important for transport, and these should be faithfully reproduced by the model.

Transport simulations are run by placing test charges along one wall of the region of interest. The wall is treated as a reflecting boundary. An electric field is applied that drives charges toward the opposite wall. Each charge alternates between making on-chain and interchain moves, where each on-chain move is actually a combination of many on-chain moves evaluated using Eq. 8. Charges are absorbed when they reach the opposite wall, and simulations usually last until all charges have done so. Since charges are assumed to be noninteracting, running a single simulation with 100 charges is the same as running 100 simulations with one charge each. When studying short-time or low-field behavior, the presence of a hard boundary can lead to errors due to biased diffusion. Thus, when computing mobility values, charges are placed 50 nm from the starting wall to mitigate this effect.

As with the structural model, the charge transport model is widely applicable. Two key assumptions are constant interchain hopping rate and noninteracting charges, both of which are imperfect but should be a good approximation for many polymer transistors. Additionally, the model here assumes that on-chain hops are independent events, but a more-complex on-chain transport model could be used by modifying Eq. 6 and computing the corresponding rates.

Data, Materials, and Software Availability. Code and data for this study are archived at DOI 10.5281/zenodo.6585396 (28).

[Images and simulations; data and code] data have been deposited in [zenodo] (10.5281/zenodo.6585396).

ACKNOWLEDGMENTS. Work at the Molecular Foundry was supported by the Office of Science, Office of Basic Energy Sciences, of the US Department of Energy under contract No. DE-AC02-05CH11231. Use of the Stanford Synchrotron Radiation Lightsource, Stanford Linear Accelerator Center National Accelerator Laboratory, is supported by the US Department of Energy, Office of Science, Office of Basic Energy Sciences under contract No. DE-AC02-76SF00515. A.S. and L.B. gratefully acknowledge financial support from the NSF, award DMR-1808401. Financial support by the Office of Naval Research under award N00014-19-1-2453 is acknowledged by L.B. for support to develop computation techniques for TEM data analysis. A.J.S. was supported by the NSF program Condensed Matter and Materials Theory (DMR-1855334).

Author affiliations: ^aDepartment of Materials Science and Engineering, Stanford University, Stanford, CA 94305; ^bDepartment of Physics, Stanford University, Stanford, CA 94305; ^cNational Center for Electron Microscopy, Molecular Foundry, Berkeleyab, Berkeley, CA 94720; ^cStanford Synchrotron Radiation Lightsource, Stanford Linear Accelerator Center National Accelerator Laboratory, Menlo Park, CA 94025; ^cDepartment of Chemical Engineering, Stanford University, Stanford, CA 94305; and ^cBiophysics Program, Stanford University, Stanford, CA 94305; and ^cBiophysics Program, Stanford University, Stanford, CA 94305;

- L. Biniek, N. Leclerc, T. Heiser, R. Bechara, M. Brinkmann, Large scale alignment and charge transport anisotropy of pBTTT films oriented by high temperature rubbing. *Macromolecules* 46, 4014–4023 (2013).
- B. A. Collins et al., Polarized X-ray scattering reveals non-crystalline orientational ordering in organic films. Nat. Mater. 11, 536-543 (2012).
- W. F. Pasveer et al., Unified description of charge-carrier mobilities in disordered semiconducting polymers. Phys. Rev. Lett. 94, 206601 (2005).
- C. J. Takacs et al., Remarkable order of a high-performance polymer. Nano Lett. 13, 2522–2527 (2013).
- K. C. Bustillo et al., 4d-stem of beam-sensitive materials. Acc. Chem. Res. 54, 2543–2551 (2021).
- C. Ophus, P. Ercius, M. Sarahan, C. Czarnik, J. Ciston, Recording and using 4d-stem datasets in materials science. *Microsc. Microanal.* 20, 62–63 (2014).
- O. Panova et al., Diffraction imaging of nanocrystalline structures in organic semiconductor molecular thin films. Nat. Mater. 18, 860-865 (2019).
- R. Noriega, A. Salleo, A. J. Spakowitz, Chain conformations dictate multiscale charge transport phenomena in disordered semiconducting polymers. *Proc. Natl. Acad. Sci. U.S.A.* 110, 16315–16320 (2013).
- R. Noruzi, E. Lim, B. S. S. Pokuri, M. L. Chabinyc, B. Ganapathysubramanian, A graph based approach to model charge transport in semiconducting polymers. npj Comput. *Mater* 8, 38 (2022).
- P. Ercíus, F. Niekiel, ncempy version 1.8.1 (2017). https://pypi.org/project/ncempy/1.8.1/. Accessed 15 January 2021.
- A. R. Chew et al., Unraveling the effect of conformational and electronic disorder in the charge transport processes of semiconducting polymers. Adv. Funct. Mater. 28, 1804142 (2018).

- 23. B. W. Boudouris *et al.*, Real-time observation of poly(3-alkylthiophene) crystallization and correlation with transient optoelectronic properties. *Macromolecules* **44**, 6653–6658 (2011).
- E. F. Koslover, A. J. Spakowitz, Discretizing elastic chains for coarse-grained polymer models. Soft Matter 9, 7016–7027 (2013).
 E. F. Koslover, A. J. Spakowitz, Systematic coarse-graining of microscale polymer models as effective elastic chains. Macromolecules 46, 2003–2014 (2013).

- L. H. Zhao et al., Role of borderline solvents to induce pronounced extended-chain lamellar order in pi-stackable polymers. Macromolecules 44, 9692–9702 (2011).
 R. A. Marcus, On the theory of oxidation-reduction reactions involving electron transfer. i. J. Chem. Phys. 24, 966–978 (1956).
 L. Balhorn et al., Data and Code For: Closing the loop between microstructure and charge transport in conjugated polymers by combining microscopy and simulation. [Data set]. Zenodo. https://doi.org/10.5281/zenodo.6585396. Deposited 26 May 2022.